Hindawi
Mathematical Problems in Engineering
Volume 2017, Article ID 7897614, 9 pages
https://doi.org/10.1155/2017/7897614

Research Article

Numerical Investigation of the FSI Characteristics in a Tubular Pump

Shuo Wang, Liaojun Zhang, and Guojiang Yin

College of Water Conservancy and Hydropower Engineering, Hohai University, Nanjing 210098, China

Correspondence should be addressed to Shuo Wang; qqwang@hhu.edu.cn

Received 18 January 2017; Revised 12 May 2017; Accepted 29 May 2017; Published 13 July 2017

Academic Editor: Haifei Liu

Flow condition was simulated in a shaft tubular pump by using the Shear-Stress Transport (SST) k-ω turbulence model with high quality structured grids in design condition. Corresponding structural vibration characteristics were then analyzed based on two-way coupled Fluid-Structure Interaction (FSI) method. Fluid results showed that flow in the outlet flow passage was a combination of the axial flow and circumferential rotation motion. Time and frequency domain analysis of pressure pulsation of typical measure points indicated that larger pulsation amplitudes appeared in the tip of the blades and the main vibration source was the pressure pulsation induced by rotation of the blades. The fluid pulsation amplitudes decreased gradually along the flow direction, which can be ascribed to the function of fixed guide vane. Structural analysis of the blades in both pressure and suction side indicated that significant stress concentration was formed at the blade and hub connection near the leading edge. Maximum effective stress of the blades varied periodically, so prevention measures of the fatigue of blades should be taken. This research can provide important reference for the design of the tubular pump.

1. Introduction

Rapid development of the industry and agriculture puts great demand on the water conservancy facilities, which gives rise to more pumping stations. Because of its less hydraulic loss, high efficiency, and compact structure, convenient installation, and maintenance, tubular pump, a kind of axial flow pump, presents wide popularity and development potential worldwide. Nevertheless, it is a bit difficult for the design and performance prediction of the tubular pump. Experimental model testing is one of the solutions for performance prediction but it is costly and time-consuming [1]. By contrast, numerical simulation is a powerful tool to provide information of the fluid flow behavior accurately, thus helping the scholars to obtain a thorough performance evaluation of a specific design [2–4].

Numerous CFD simulations were performed to analyze the flow features of the pump and then corresponding optimization design was provided. Jafarzadeh et al. [3] presented a general three-dimensional simulation of a high-speed centrifugal pump to predict velocity and pressure field. The optimum pumping operation was explored in terms of turbulence models and the number of blades. Shojaeefard et al. [5] investigated the effects of the blade outlet angle and passage width on the centrifugal pump performance during the pumping of water and oil, and they found pump head and efficiency can be increased with a proper modification of the original geometry. Zhu et al. [6] applied a multiobjective optimization design system to the design of a middle-high-head pump-turbine runner and concluded that the choice of blade loading and the meridional channel shape is crucial to efficiency and operation stability. All their researches have beneficial enlightenment, but without taking the coupled effect of the fluid and solid into account, their concern is mainly the fluid feature.

Analysis of the stress distribution characteristics of a centrifugal pump was conducted in [7, 8]. Results showed that the maximum stress on the blade appeared on the pressure side near the hub, and the maximum static stress increased with the decreasing of the flow rate. However, like previously mentioned researches, they focused on the centrifugal pump, and enough importance was not attached to the axial flow pump.

Shi and Wang [9], Tang et al. [10], and Zhang et al. [11] calculated the stress and deformation of the axial impeller and

found similar law of stress and deformation distribution. But guide vanes and tip clearance were omitted for simplification in their structure simulation, which could not reflect the actual characteristics of the pump. There is tremendous need for the detailed study of the axial flow pump based on two-way coupled Fluid-Structure Interaction approach [12].

On account of the scarcities above, this research performed simulation of the actual flow in a shaft tubular pump to acquire the general features of the fluid flow and vibration characteristics of the blades in design condition. Based on two-way coupled FSI approach, a three-dimensional unified model for a shaft tubular pump was established, including the whole flow passage, the structure of the impeller, and the fixed guide vane. Analysis of flow pattern was performed using the SST k-ω turbulence model to obtain the general law in the flow passage. Time and frequency domain analysis of the fluid pressure pulsation was conducted to explore its vibration characteristics. For the structure, features of effective stress, strain, deformation, and velocity distribution in both pressure and suction sides of the blades were analyzed and the property of maximum dynamic stress was evaluated. Note that the whole calculation was performed with the commercial software ADINA.

2. Basic Theory and Method

2.1. Basic Equations. For the fluid flow analysis, the continuity equation and Reynolds-Averaged Navier–Stokes equation for an incompressible flow have been used in the following form [13]:

$$\begin{aligned} \frac{\partial u_j}{\partial x_j} &= 0, \\ \frac{\partial u_i}{\partial t} + u_j \frac{\partial u_i}{\partial x_j} &= -\frac{1}{\rho}\frac{\partial p}{\partial x_i} + \upsilon \frac{\partial^2 u_i}{\partial x_j \partial x_i} - \frac{\partial}{\partial x_j}\left(\overline{u_i' u_j'}\right) + f_i, \end{aligned} \tag{1}$$

where u_i is an average velocity component, and $\overline{u_i' u_j'}$ is the turbulent stress. In this research Shear-Stress Transport (SST) k-ω turbulence model proposed by Menter is used to acquire the features of unsteady flow in CFD calculation. SST k-ω turbulence model can yield more accurate and reliable results for simulating flows with adverse pressure gradient [14], flows around complex geometry [15], transonic flows [16], and so forth. Equation for SST k-ω turbulence model is expressed as follows [17–19]:

$$\begin{aligned} \rho\frac{\partial k}{\partial t} + \rho\frac{\partial}{\partial x_j}\left(k u_j\right) &= \frac{\partial}{\partial x_j}\left(\Gamma_k \frac{\partial k}{\partial x_j}\right) + \overline{G}_k - Y_k + S_k, \\ \rho\frac{\partial \omega}{\partial t} + \rho\frac{\partial}{\partial x_j}\left(\omega u_j\right) &= \frac{\partial}{\partial x_j}\left(\Gamma_\omega \frac{\partial \omega}{\partial x_j}\right) + G_\omega - Y_\omega + D_\omega \\ &\quad + S_\omega, \end{aligned} \tag{2}$$

where k and ω are turbulent kinetic and turbulence dissipation rate, respectively, $\overline{G}_k$ is a productive term of the turbulent kinetic, G_ω is a productive term of the turbulence dissipation rate, Γ_k and Γ_ω are the effective diffusion coefficients of k and ω, respectively, Y_k and Y_ω are the dissipation terms of k and ω, respectively, D_ω is the cross-diffusion term, and S_k and S_ω are source terms.

The fundamental conditions applied to the FSI [20] are the kinematic condition (or displacement compatibility) and the dynamic condition (or traction equilibrium), and corresponding equations are expressed in (3) and (4), respectively.

$$\underline{d}_f = \underline{d}_s, \tag{3}$$

$$n \cdot \underline{\tau}_f = n \cdot \underline{\tau}_s, \tag{4}$$

where $\underline{d}_f$ and $\underline{d}_s$ are, respectively, the fluid and solid displacements, and $\underline{\tau}_f$ and $\underline{\tau}_s$ are, respectively, the fluid and solid stresses. The underlining denotes that the values are defined on the fluid-structure interfaces only.

When no-slip or slip condition is applied separately, the fluid velocity condition that resulted from the kinematic condition is expressed in (5) and (6), respectively.

$$\underline{v} = \dot{\underline{d}}_s, \tag{5}$$

$$n \cdot \underline{v} = n \cdot \dot{\underline{d}}_s. \tag{6}$$

Fourier analysis is employed in vibration analysis of the pressure pulsation in fluid domain and dynamic stress in solid domain. Given a time history $f(t)$, defined from t_0 to t_1, the Fourier series corresponding to $f(t)$ is expressed as follows:

$$f(t) = a_0 + \sum_{n=1}^{\infty}\left(a_n \cos n\omega_1 t + b_n \sin n\omega_1 t\right), \tag{7}$$

where $\omega_1 = 2\pi/t_p$, $t_p = t_1 - t_0$, $a_0 = (1/t_p)\int_{t_0}^{t_1} f(t)dt$, $a_n = (2/t_p)\int_{t_0}^{t_1} f(t)\cos n\omega_1 t\, dt$, $b_n = (2/t_p)\int_{t_0}^{t_1} f(t)\sin n\omega_1 t\, dt$.

Equation (7) could be rewritten as (8) due to sine and cosine transforms:

$$f(t) = c_0 + \sum_{n=1}^{\infty} c_n \cos\left(n\omega_1 t - \Phi_n\right), \tag{8}$$

where $c_n = \sqrt{a_n^2 + b_n^2}$, $\Phi_n = \tan^{-1}(b_n/a_n)$.

Conceptually, the function $f(t)$ is considered to contain the frequencies $0, \omega_1, 2\omega_1, \ldots$. The constants c_n and Φ_n are the amplitude and phase angle of that portion of $f(t)$ which oscillates at frequency $n\omega_1$.

2.2. Numerical Model. A unified finite element model was established to analyze the coupled vibration of the pump. The fluid domain, as shown in Figure 1, is composed of inlet flow passage, an impeller chamber, a guide vane chamber, a water-guide cone, and outlet flow passage. The solid domain, as shown in Figure 2, contains impeller, guide vanes, water-guide cone, and shaft. The geometric parameters of the pump model are as follows: impeller diameter $D_2 = 3.25$ m, flow rate in design condition $Q = 30\ \mathrm{m}^3/\mathrm{s}$, rated head $H = 1.96$ m, rated rotation speed $n = 105$ rpm, and rotation frequency $f_n = 105/60 = 1.75$ Hz. The number of impeller blades is 3, and the number of guide vanes is 5. Tip clearance is

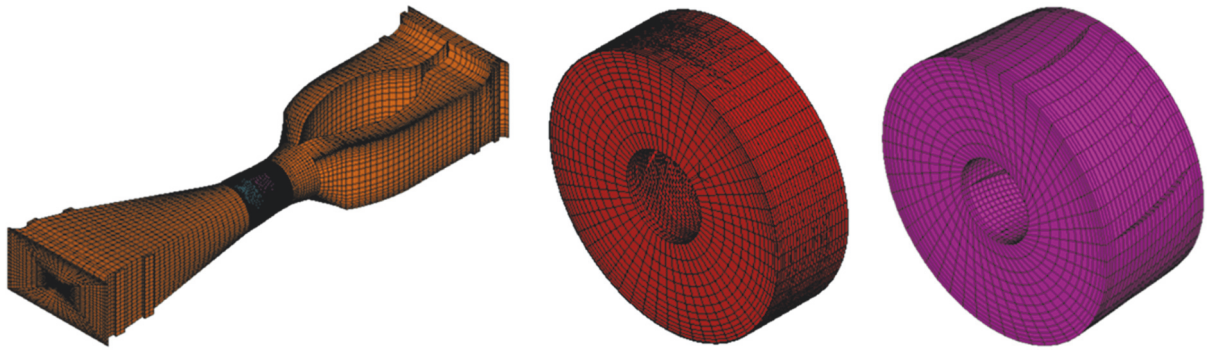

(a) Integral flow passage (b) Water around impeller (c) Water around guide vanes

Figure 1: Structured grids for fluid domain.

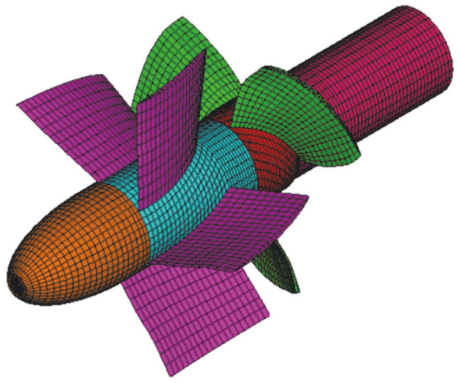

Figure 2: Structured grids for solid domain.

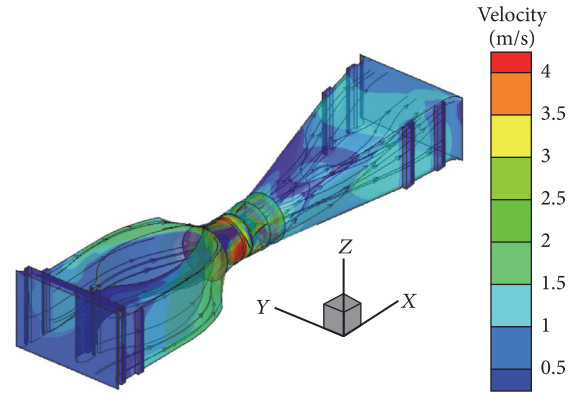

Figure 3: Three-dimension distribution of velocity magnitude and streamlines.

considered and the value is 5 mm. Density for fluid and solid is 1000 and 7850 kg/m^3, respectively. Structured grids are chosen and designed on the basis of different topology and finer grids are applied to the rotational zone and field near the wall to ensure high-accuracy results. For most of the first cells near the wall, the $y+$ values are in the variation of 30 to 500 to ensure correct utilization of the model. Mass convergence criteria are adopted in equation residual with a tolerance of 0.0001. For this study, the chosen computation is comprised of 123519 grid nodes and 106892 elements in fluid domain, including 25536 elements in inlet flow passage, 23964 elements in an impeller chamber, 15600 elements in the guide vane chamber, 16192 elements in the water-guide cone, and 25600 elements in outlet flow passage, and 24690 grid nodes and 18230 elements in solid domain, including 4680 elements in impeller, 6320 elements in guide vanes, 3000 elements in water-guide cone, and 4230 elements in shaft.

The FSI simulation is carried out in design condition with blades rotating under dynamic operation. The inlet boundary condition is set as a uniform velocity of 0.575 m/s in terms of the flow rate 30 m^3/s, normal to the inlet. Fully developed turbulent flow is supposed at the outlet and outflow is defined as the outlet boundary condition. The rotational speed of 105 rpm is assigned to the impeller, where the sliding mesh boundary condition is employed to satisfy the compatibility, continuity, and completeness conditions along the nonconforming interfaces. Wall boundary condition is imposed on the outmost layer of the flow body with no-slip velocity assumed. For the interface between fluid and structure, FSI boundary condition is assigned to make the mutual transmission of velocity and pressure.

The commercial software ADINA is adopted to study the performance of the pump under transient state in ADINA CFD module and dynamic-implicit analysis in ADINA structure module. The entire fluid domain of the pump is formed by combining the components with an interface between impeller and guide vanes. Total calculation time is set as 10 seconds to obtain reliable simulation results. There are 2000 steps calculated and the time step is 0.005 seconds.

3. Analysis of the Results

3.1. Fluid Vibration Analysis

3.1.1. Analysis of Flow Pattern. Figure 3 presents the velocity distribution band and three-dimensional streamlines in the flow passage at $t = 10$ s and Figure 4 is close look in typical sections. With steady flow pattern, there is no reflux in the inlet flow passage during the pump operation. The velocity increased greatly and the flow pattern remains steady as

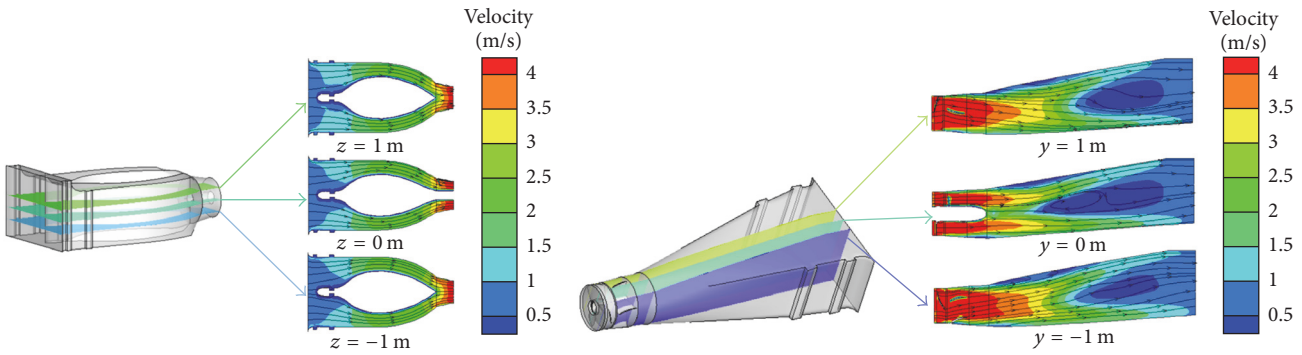

(a) Three horizontal sections in the inlet flow passage ($z = -1$ m, 0 m, 1 m)

(b) Three vertical sections in the outlet flow passage ($y = -1$ m, 0 m, 1 m)

Figure 4: Distribution of velocity magnitude and streamlines in typical sections.

Table 1: First main frequency and amplitude of measure points.

Measure points	Before impeller				Between impeller and guide vanes				Behind water-guide cone			
	P11	P12	P13	P14	P21	P22	P23	P24	P31	P32	P33	P34
First main frequency (Hz)	5.25	5.25	5.25	5.25	5.25	5.25	5.25	5.25	1.50	1.50	1.50	1.50
Amplitude (Pa)	3371	3251	2437	1785	2321	2087	1383	1040	754	762	773	781

the water flows into the impeller. Although most circulation generated by the work of impeller is rectified and recovered by the fixed guide vane, there is still certain velocity circulation and reflux in the outlet flow passage, which can also be ascribed to the diffuse type of the outlet flow passage. The streamlines deflect in the outermost section and have friction with the pump casing. In total, the design of the pump flow channel is reasonable, so the stability and safety of operation can be guaranteed.

3.1.2. Analysis of Fluid Pressure Pulsation. Vibration analysis of pressure pulsation enhances both hydraulic and dynamic performance and assures safety and reliability of the pumping station. As shown in Figure 5, four measure points are chosen along the radius direction to conduct vibration response analysis in time and frequency domain, the locations of which are from blade tip to hub, respectively. The measure sections where the measure points are placed are before the impeller, between impeller and the guide vanes, and behind the water-guide cone.

Time history curves and spectrum analysis of pressure pulsation are presented in Figures 6–8 and first main frequency and amplitude are shown in Table 1. Since fluctuation of the nodal pressure remains periodically steady at about $t = 6$ s, the regularity of pressure pulsation is analyzed within the time range of $t = 6$ s to $t = 10$ s. It is clear that the pressure pulsation of the measure points at the same cross section has the similar trend. For the section before impeller, the pressure magnitude varies between 30000 Pa and 44000 Pa and increases with less amplitude from tip to hub with a dominant frequency of 5.25 Hz, shown in Figure 6(b), which equals the product of blades number 3 and rotation frequency 1.75 Hz. Pressure magnitude of the

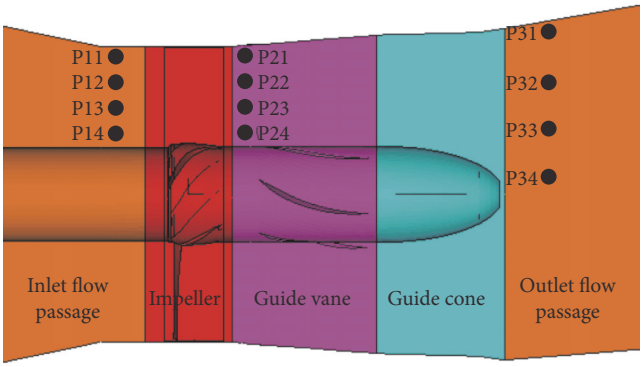

Figure 5: Measure point distribution in the flow passage of the pump.

measure points between impeller and guide vanes varies between 40000 Pa and 50000 Pa and has similar vibration features, which illustrates that the pulsation is mainly caused by blades rotation. For the section after water-guide cone, the pressure magnitude varies between 47000 Pa and 51000 Pa and decreases with more amplitude from tip to hub with a dominant low frequency of 1.50 Hz, illustrated in Figure 8(b).

When analyzing these measure points together, we find that the pulsation amplitudes decrease gradually along the flow direction; that is, the pressure pulsation amplitude before the impeller is larger than that between impeller and the guide vanes, and both amplitudes of them are larger than that behind the water-guide cone. Due to the

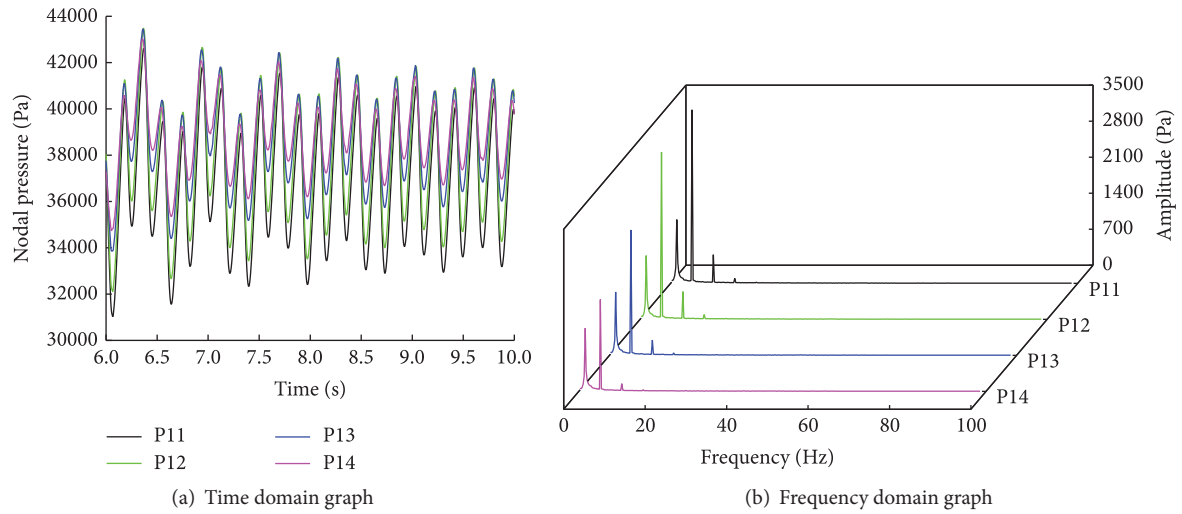

(a) Time domain graph (b) Frequency domain graph

Figure 6: Pressure pulsation analysis of measure points before the impeller (P11–P14).

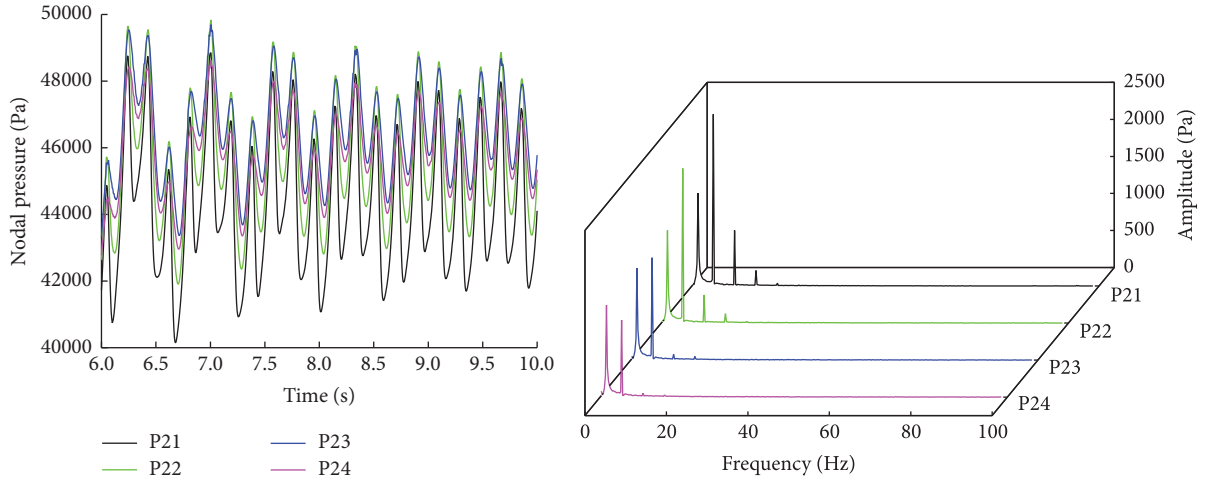

(a) Time domain graph (b) Frequency domain graph

Figure 7: Pressure pulsation analysis of measure points between impeller and the guide vanes (P21–P24).

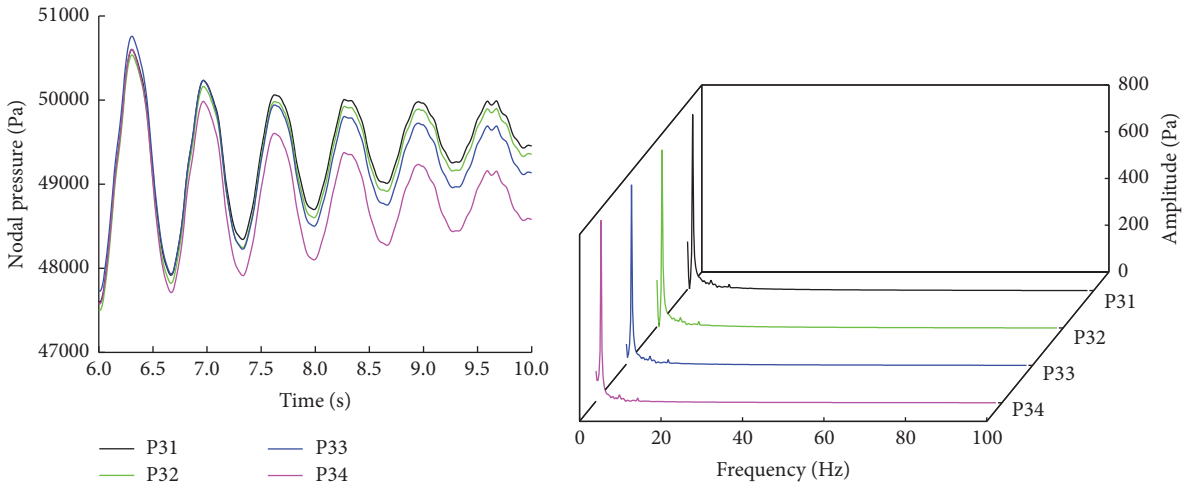

(a) Time domain graph (b) Frequency domain graph

Figure 8: Pressure pulsation analysis of measure points behind water-guide cone (P31–P34).

Table 2: Main frequency and amplitude of maximum effective stress of the blades.

Frequency (Hz)	0.25	1.75	3.5	7	8.75
Amplitude (MPa)	0.19	0.43	0.25	0.17	0.12
Multiple of the rotating frequency 1.75 Hz	Low frequency	1	2	4	5

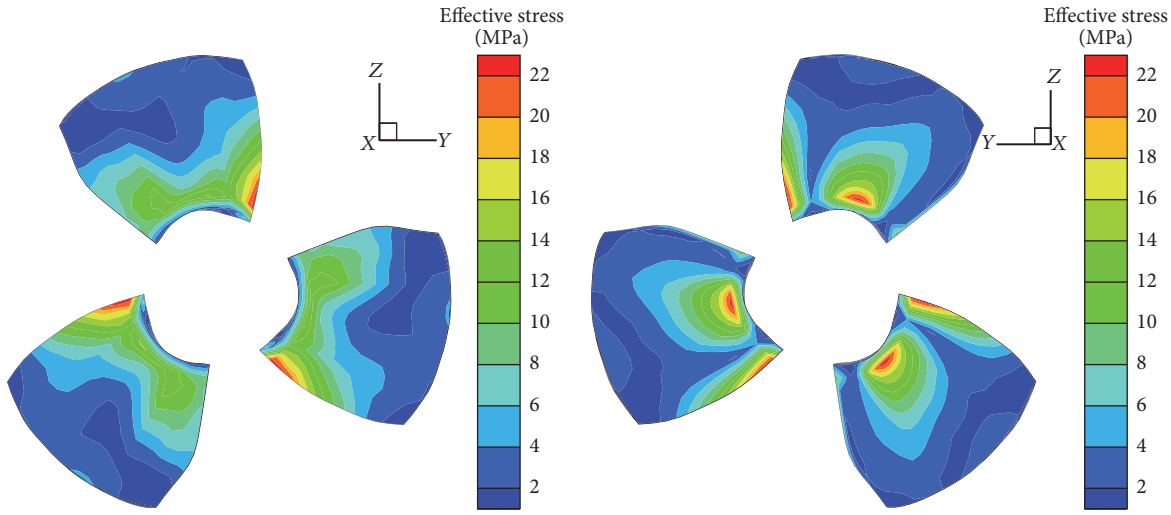

(a) Pressure side (b) Suction side

Figure 9: Effective stress distribution of the blades.

constraint function of the guide vanes, the pressure tends to be stable and the pulsation amplitude is greatly reduced. Great attention should be paid to the inlet of the impeller chamber in future hydraulic design as the disturbance of the blades has already existed before the water flowed into the impeller.

3.2. Structural Vibration Analysis

3.2.1. Effective Stress and Strain Analysis of the Blades. For pump design, the major mission is to analyze the structural response to the flow induced excitation and diagnose the faults early. Figure 9 shows the effective stress distribution of the blades in both pressure and suction side at $t = 10$ s in dynamic design operation. The maximum effective stress of blades is 23.59 MPa, appearing at the blade root near the leading edge. Because of the huge flow impact generated in the leading edge of the blades, the stress concentration is formed and it is prone to crack and fracture. The effective stress distribution basically declines from the joint of the blade root to the trailing edge and the tip, where the stress is much lower. Figure 10 is the corresponding strain at $t = 10$ s. The distribution of the strain is coincident with that of the stress.

3.2.2. Deformation Analysis of the Blades. Figure 11 is the deformation distribution of the blades at $t = 10$ s in dynamic design operation. The deformation magnitude augments with the increase of the radius in both pressure and suction side. On account of the larger centrifugal force, thinner thickness, and insufficient rigidity of the tip, the maximum deformation appears at the blade tip, which is consistent with the result of the maximum effective stress distribution.

3.2.3. Velocity Analysis of the Blades. Velocity distribution of the blades at $t = 10$ s in dynamic design operation is shown in Figure 12. We can see that velocity increases gradually with the increase of radius. The maximum velocity magnitude appears at the blade tip, which is coincident with the manual calculation result; that is, $v = \omega \cdot r = 10.99 \times 1.625 = 17.86$ m/s.

3.2.4. Dynamic Stress Analysis of the Blades. Figure 13 is the time history curve and Fourier frequency analysis of maximum effective stress of the blades and Table 2 is corresponding magnitude of the main frequency and amplitude. It is clear that the maximum effective stress changes periodically as time changes, with magnitude varying between 22 and 25 MPa. Frequency analysis illustrated in Figure 13(b) and Table 2 shows that the first main frequency of the maximum effective stress is 1.75 Hz, and the corresponding amplitude is 0.43 MPa, which illustrates the periodically varying stress is mainly influenced by the rotational frequency of impeller. The static stress can not make the blades damaged because the value of maximum effective stress is much less than the limit stress of material. However, practice shows that the alternating stress could cause abrupt fracture of the structure with no significant plastic deformation before occurrence of fracture, even if the stress magnitude is much lower than the yield limit. Therefore, prevention measures of the fatigue of impeller should be taken due to the period variation of the effective stress.

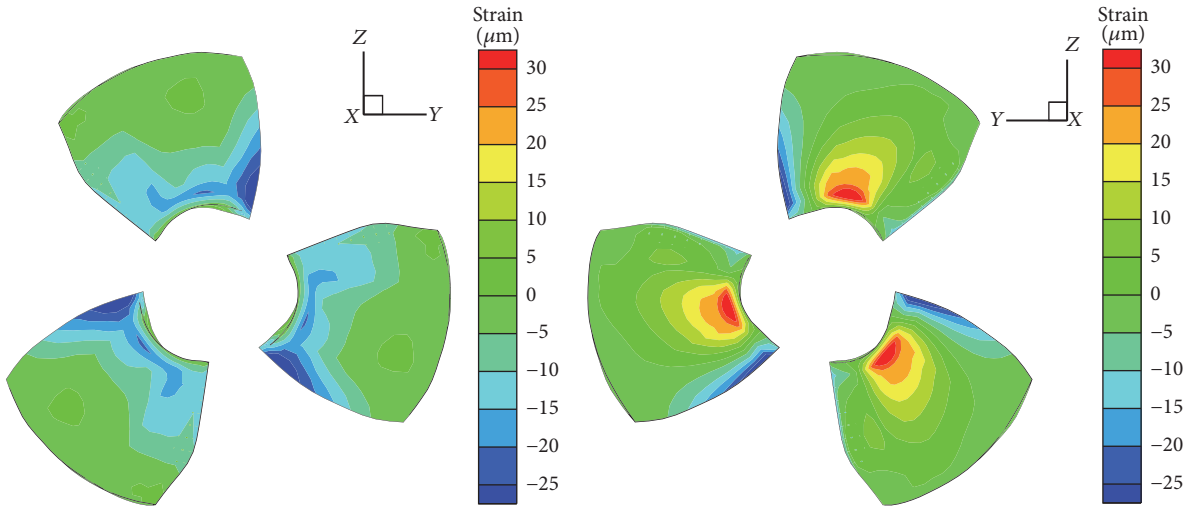

(a) Pressure side (b) Suction side

Figure 10: Strain distribution of the blades.

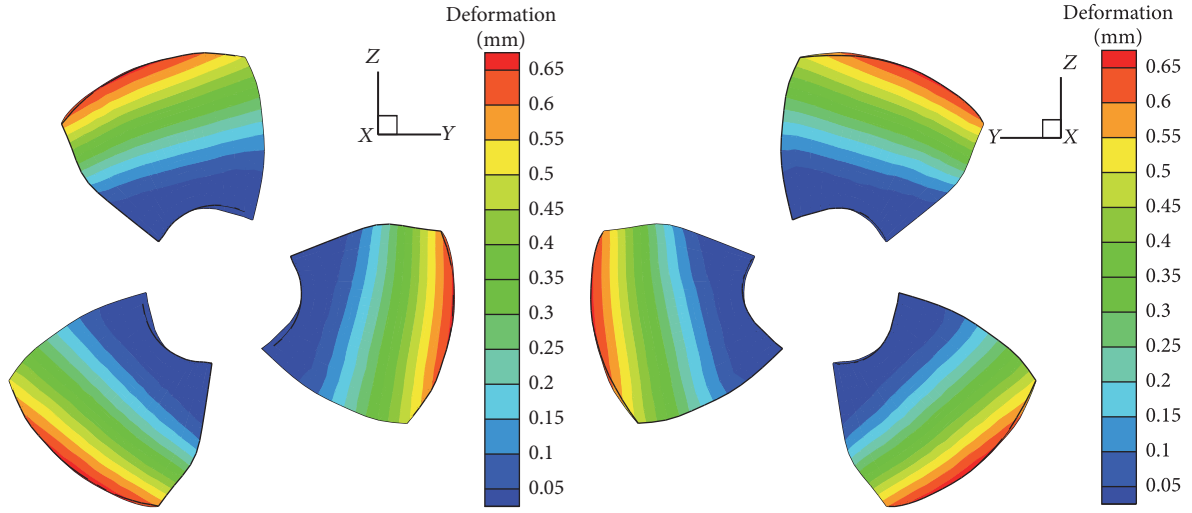

(a) Pressure side (b) Suction side

Figure 11: Deformation distribution of the blades.

4. Conclusion

In present investigation, numerical simulation of flow condition in a shaft tubular pump was performed and the vibration characteristics of the blades in design condition were analyzed. The numerical method was based on the SST k-ω turbulence model and the two-way coupled FSI approach under transient state. The following conclusions can be made by analysis of the results:

(1) The flow pattern is steady in the inlet flow passage in design condition. Due to the incomplete recovery of the flow circulation by the fixed guide vane and the diffusion shape of the outlet flow passage, vortex occurs in the center and the streamlines deflect in the outer section of the outlet flow passage, which illustrates that the flow in outlet flow passage is a combination of the axial flow and circumferential rotation motion. In total, the design of the pump flow channel is rational and the stability and safety of operation can be guaranteed.

(2) Time and frequency domain analysis shows that the fluid pressure magnitude increases with less amplitude from blade tip to hub before impeller and between impeller and guide vanes with a dominant frequency of 5.25 Hz. The fluid pressure magnitude decreased with more amplitude from tip to hub after water-guide cone, and its dominant frequency is 1.50 Hz. Larger pulsation amplitudes appear in the tip of the blades, which indicates that optimizing the airfoil shape and structural parameters of the blade tip is an important way to improve the pressure pulsation condition in pump operation. The dominant frequency shows the main vibration source in fluid flow is the pressure pulsation induced by blade rotation. The pulsation amplitude decreases along the flow direction

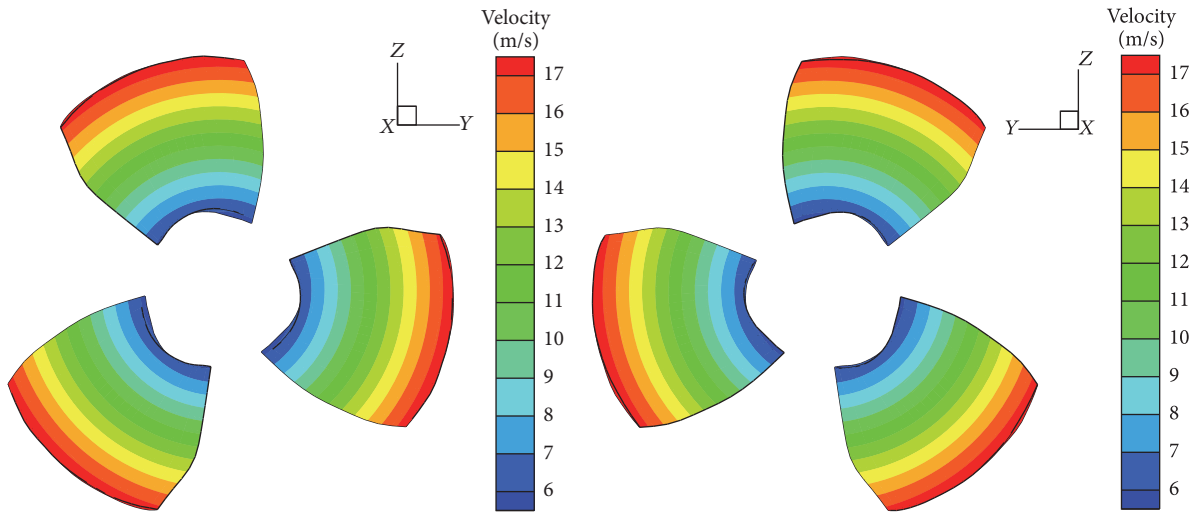

(a) Pressure side (b) Suction side

Figure 12: Velocity distribution of the blades.

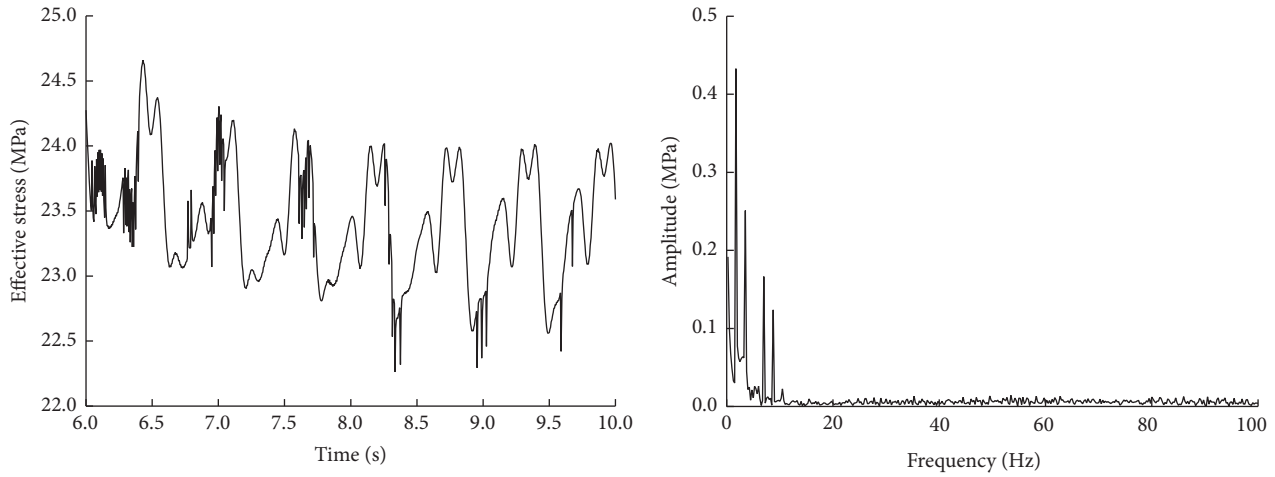

(a) Time domain graph (b) Frequency domain graph

Figure 13: Time and frequency domain graph of maximum effective stress of the blades.

with the maximum before the impeller, which illustrates that the fixed guide vane has a function of restricting pressure pulsation and greatly improving the flow pattern in the pump.

(3) Analysis of the stress, strain, deformation, and velocity distribution of the blades is performed based on FSI. The result demonstrates that the maximum effective stress occurs between blade and hub near the leading edge, which requires the designers to attach importance to the strength check of the root. The stress at trailing edge and the tip is comparatively smaller, which is coincident with the result of strain. The tip has maximum deformation, which is prone to friction damage of the blade tip and pump casing because of the tiny clearance between them. Maximum velocity occurs at the tip, which is coincident with the manual calculation results. Although the value of maximum effective stress is much less than the yield limit, prevention measures of the fatigue of impeller should be taken due to the period variation of the effective stress.

Conflicts of Interest

The authors declare that they have no conflicts of interest.

Acknowledgments

This work was supported by the Priority Academic Program Development of Jiangsu Higher Education Institutions.

References

[1] S. R. Shah, S. V. Jain, R. N. Patel, and V. J. Lakhera, "CFD for centrifugal pumps: A review of the state-of-the-art," in *Proceedings of the 3rd Nirma University International Conference*

on Engineering, NUiCONE 2012, pp. 715–720, ind, December 2012.

[2] L. Deyou, W. Hongjie, X. Gaoming, G. Ruzhi, W. Xianzhu, and L. Zhansheng, "Unsteady simulation and analysis for hump characteristics of a pump turbine model," *Renewable Energy*, vol. 77, pp. 32–42, 2015.

[3] B. Jafarzadeh, A. Hajari, M. M. Alishahi, and M. H. Akbari, "The flow simulation of a low-specific-speed high-speed centrifugal pump," *Applied Mathematical Modelling*, vol. 35, no. 1, pp. 242–249, 2011.

[4] H.-J. Choi, M. A. Zullah, H.-W. Roh, P.-S. Ha, S.-Y. Oh, and Y.-H. Lee, "CFD validation of performance improvement of a 500 kW Francis turbine," *Renewable Energy*, vol. 54, pp. 111–123, 2013.

[5] M. H. Shojaeefard, M. Tahani, M. B. Ehghaghi, M. A. Fallahian, and M. Beglari, "Numerical study of the effects of some geometric characteristics of a centrifugal pump impeller that pumps a viscous fluid," *Computers and Fluids*, vol. 60, pp. 61–70, 2012.

[6] B. Zhu, X. Wang, L. Tan, D. Zhou, Y. Zhao, and S. Cao, "Optimization design of a reversible pump-turbine runner with high efficiency and stability," *Renewable Energy*, vol. 81, pp. 366–376, 2015.

[7] F. F. Hu, T. Chen, D. Z. Wu, and L. Q. Wang, "Computation of stress distribution in a mixed flow pump based on fluid-structure interaction analysis," in *Proceedings of the 6th International Conference on Pumps and Fans with Compressors and Wind Turbines, ICPF 2013*, chn, September 2013.

[8] J. Pei, S. Yuan, and J. Yuan, "Dynamic stress analysis of sewage centrifugal pump impeller based on two-way coupling method," *Chinese Journal of Mechanical Engineering (English Edition)*, vol. 27, no. 2, pp. 369–375, 2014.

[9] W. Shi and G. Wang, "Finite element computation for impeller of axial-flow pump based on fluid-structure interaction," in *Proceedings of the 2nd Annual Conference on Electrical and Control Engineering, ICECE 2011*, pp. 3935–3938, chn, September 2011.

[10] X. Tang, Y. Jia, F. Wang et al., "Turbulent flows in tubular pump and fluid-structure interaction characteristics of impeller," *Paiguan Jixie Gongcheng Xuebao/Journal of Drainage and Irrigation Machinery Engineering*, vol. 31, no. 5, pp. 379–383, 2013.

[11] X. Zhang, Y. Zheng, X. Mao, W. U. Zaiqiang, K. Kan, and T. Mou, *Strength Analysis of Axial Flow Pump Impeller Based on Fluid Solid Coupling*, Water Resources Power, 2014.

[12] C. Trivedi and M. J. Cervantes, "Fluid-structure interactions in Francis turbines: A perspective review," *Renewable and Sustainable Energy Reviews*, vol. 68, pp. 87–101, 2017.

[13] F. R. Menter, "Two-equation eddy-viscosity turbulence models for engineering applications," *AIAA journal*, vol. 32, no. 8, pp. 1598–1605, 1994.

[14] J. Li, C. Zhong, D. Pan, and C. Zhuo, "A gas-kinetic scheme coupled with SST model for turbulent flows," *Computers and Mathematics with Applications*, 2016.

[15] S. J. Kim, J.-S. Jung, and S. Kang, "Fully three-dimensional Reynolds-averaged Navier–Stokes modeling for solving free surface flows around coastal drainage gates," *Journal of Hydro-Environment Research*, vol. 13, pp. 121–133, 2016.

[16] J. Gao, Q. Zheng, X. Niu, and G. Yue, "Aerothermal characteristics of a transonic tip flow in a turbine cascade with tip clearance variations," *Applied Thermal Engineering*, vol. 107, pp. 271–283, 2016.

[17] F. Menter, "Zonal Two Equation k-w Turbulence Models For Aerodynamic Flows," in *Proceedings of the 23rd Fluid Dynamics, Plasmadynamics, and Lasers Conference*, Orlando,FL,U.S.A..

[18] F. R. Menter, M. Kuntz, and R. Langtry, Ten years of industrial experience with the SST turbulence model, Turbulence,.

[19] F. R. Menter, *Review of the shear-stress transport turbulence model experience from an industrial perspective*, Taylor Francis, Inc, 2009.

[20] S.-h. Wei and L.-j. Zhang, "Vibration analysis of hydropower house based on fluid-structure coupling numerical method," *Water Science and Engineering*, vol. 3, pp. 75–84, 2010.